Designing Visible-Light Photoactive Thioapatites Using Thiovanadate Groups: The Ba5(VO4-αSα)3X (X = F, Cl, I) Phases

Batoul Almoussawi, Smritijit Sen, Sebastien Saitzek, Pascal Roussel, Houria Kabbour

Designing visible light photoactive thio-apatites using thiovanadates groups: the $Ba_5(VO_{4-\alpha}S_\alpha)_3X$ (X= F, Cl, I) phases

Batoul Almoussawi[1], Smritijit Sen[1], Sébastien Saitzek[2], Pascal Roussel[1], Houria Kabbour[1, 3*]

[1] *Univ. Lille, CNRS, Centrale Lille, ENSCL, Univ. Artois, UMR 8181 – UCCS – Unité de Catalyse et Chimie du Solide, F-59000 Lille, France.*

[2] *Univ. Artois, CNRS, Centrale Lille, Univ. Lille, UMR 8181, Unité de Catalyse et Chimie du Solide (UCCS), F-62300 Lens, France*

3

*houria.kabbour@cnrs-imn.fr

Abstract

The new thio-apatite $Ba_5(VO_{4-\alpha}S_\alpha)_3X$ (X= F, Cl, I) series of compounds was prepared and characterized. Compared to known apatite phases built from unconnected vanadate VO_4 groups separated by Ba^{2+} cations delimiting halide-filled channels, their crystal structure is built from mixed anion thiovanadates $VO_{4-\alpha}S_\alpha$, where V^{5+} is surrounding by both O and S, therefore exhibiting a triple anion lattice. Here, the strategy consisting in incorporating a chalcogenide anion aims at raising the valence band to bring the band gap to the visible range, in order to reach photoactive materials under visible light. Both the halide anion nature and the S/O ratio impact the materials photoconductivity. While the photocurrent response is comparable to that found in the recently investigated apatite phase $Pb_5(VO_4)_3I$, a short carrier lifetime is detected as well as a shift of the activity toward the visible-light. This apatite series combining thiovanadates and halide-filled channels open new perspectives in the extended field of apatites and their applications.

Keywords

Mixed anion, apatite, thiovanadate, oxychalcogenide, halide, optical properties, photocurrent, band gap engineering

Introduction

Anionic species, by their characteristic differentiation, can afford unusual properties to mixed anion compounds. The large range of properties found among mixed anion compounds (superconductivity[1], non-linear optical[2], thermoelectric[3], magnetic[4], …) make them suitable for functional materials design[5]. Theoretical calculations show that the valence band maximum is dictated mainly by hybridized orbital anions. A less electronegative anion will raise the valence band maximum. Therefore, they offer great possibilities to engineer the band gap by anionic manipulation. Beside oxynitrides[6] known for decades now to present a photocatalytic activity for water-splitting in the visible range, a few oxysulfides have recently shown promising activities while being stable[6,7] like in $Y_2Ti_2O_5S_2$[7] and $LaOInS_2$[8]. Dealing with oxychalcogenides, a few low-dimensional compounds are reported with thiovanadates. They constitute a great playground for band gap engineering based on the thiovanadate[9] species with all possible S/O ratios[10]. For example, in $Ba_6V_4O_5S_{11}$, the formula of which can be decomposed as $Ba_6(VO_2S_2)_2(VS_3O)(VS_4)$, the density of states projected on the various thiovanadates units shows their tendency to contribute more in the top of the valence band when the sulfur content is increased (from $VO_3S \rightarrow VS_4$)[11]. This type of heteroleptic environment (i.e. at least two types of anions around the cation) increase the local acentricity and the polarity in case of polar structures. In the latter, the increased built-in electrical field allow enhancing numerous properties including photoelectric response by allowing a better charge carrier separation[12]. However, mixed anion compounds have been barely explored to that purpose. apatites $M_{10}(AO_4)_6X_2$ (*M* and *A*: cationic sites with *A* in unconnected tetrahedral AO_4) and *X*: channel's anionic site such as a halide) are very common compounds which exhibit two anionic sites of different nature[13]. They exhibit useful properties with various practical applications such as fertilizers, food additives, and bioceramics but also as catalysts and fluorescent host materials. On another hand, $Pb_5(VO_4)X$ (*X*= F, Cl, Br, I) apatites have been recently reported[14] with light absorption properties which opens new perspectives in this family. The iodide-phase has a band gap in the visible range (2.7 eV) thanks to the contribution of the I 5*p* states at the top of the valence band which allow a response in the visible range as a photoanode for photoelectric conversion. In this work, we adopt a strategy based on the insertion of sulfide anions in oxy-halide apatites, in order to reach materials active under visible light. It leads to a new halide-thio-apatites family $Ba_5(VO_{4-\delta}S_\delta)X$ (*X*= F, Cl, Br, I) which contain thiovanadate groups instead of vanadate groups. We present their structures,

2

optical and photoelectric properties and show their potential for band gap engineering.

Experimental section

Synthesis: Powders of the phases were obtained from a stoichiometric mixture of BaO, BaX$_2$ (BaCl$_2$, BaI$_2$ or BaF$_2$), V$_2$O$_5$, V and S pressed into pellets and heated in an evacuated sealed quartz tube. After several trials, the optimal heat treatment consists in heating up to 450°C at the rate of ~20°C/h and maintaining this temperature for 5 hours, then heating up to 750°C at the rate of 30°C/h and kept at this temperature for 24 hours. The sample was finally cooled down to 650°C at a 5°C/h rate, temperature at which the furnace was switched off.

X-ray diffraction on single crystals was performed on a Bruker Apex X8 diffractometer equipped with a two-dimensional (2D) CCD 4K detector and an Ag K$_\alpha$ or Mo K$_\alpha$ source was used.

The powder XRD patterns were collected on a Bruker D8-A25 diffractometer equipped with a Lynxeye XET linear detector (Cu Kα) in Bragg−Brentano geometry at room temperature.

Scanning electron microscopy (SEM) experiments and EDX analysis were carried out on a Hitachi S400N microscope.

UV−Visible Measurements. The reflectance of the sample was measured from 250 to 800 nm on a PerkinElmer Lambda 650 device.

Photo-electrochemical Measurements. The photocurrents and Mott-Schottky plots were measured by an electrochemical device (Autolab PGSTAT204, Metrohm) coupled to a LEDmodule (LED Driver kit, Metrohm). LEDs with low spectral dispersion are calibrated with the help of a photodiode to determine the density of the luminous flux received by the sample. Three electrodes were used for the measurements, including Ag/AgCl and Pt wire acted as reference electrode and counter electrode, respectively. The working electrode was prepared using the drop-casting method. For this, 20 mg of sample is mixed with Polyvinylidene fluoride (PVDF) binder with 1:0.5 weight ratio. The homogeneous mixture is then coated on an Indium Tin Oxide (ITO) glass wafer. Finally, the photoelectrode is dried at 90°C for 30 min before being placed in a photoelectrochemical cell. The electrolyte was 0.1 M Na$_2$SO$_4$ aqueous solution (pH = 7). The Mott-Schottky curves were recorded at 1 kHz and the applied bias voltage was 0.2 V in the current-time curves.

Computational methods. Density functional theory calculations are performed by implementing the projector augmented-wave (PAW) (ref A, B) method within the Vienna ab initio simulation package (VASP) (ref C). SCAN meta-GGA (ref D, E) has been used as an exchange correlation functional for all the calculations as it appears to produce a more realistic band gap as compared to GGA. All the lattice parameters as well as atomic positions are relaxed with an energy convergence of 10^{-6} eV. The wave functions are expanded in the plane wave basis with an energy cut-off of 530 eV. The sampling of the Brillouin zone was done using a Γ-centered Monkhorst-Pack grid. Disorder has been treated within the supercell method.

(A)   Blöchl, P. E. Projector Augmented-Wave Method. Physical Review B 1994, 50 (24), 17953–17979. DOI: 10.1103/PhysRevB.50.17953.

(B)   Kresse, G.; Joubert, D. From Ultrasoft Pseudopotentials to the Projector Augmented-Wave Method. Physical Review B 1999, 59 (3), 1758–1775. DOI: 10.1103/PhysRevB.59.1758.

(C)   G. Kresse and J. Furthmüller. Efficient iterative schemes for ab initio total-energy calculations using a plane-wave basis set. Phys. Rev. B 1996, 54 , 11 169.

(D)   Tao, J.; Perdew, J. P.; Staroverov, V. N.; Scuseria, G. E. Climbing the Density Functional Ladder: Nonempirical Meta--Generalized Gradient Approximation Designed for Molecules and Solids. Phys. Rev. Lett. 2003, 91 (14), 146401. DOI: 10.1103/PhysRevLett.91.146401.

(E)   Yang, Z.; Peng, H.; Sun, J.; Perdew, J. P. More Realistic Band Gaps from Meta-Generalized Gradient Approximations: Only in a Generalized Kohn-Sham Scheme. Physical Review B 2016, 93 (20), 205205. DOI: 10.1103/PhysRevB.93.205205.

Results and Discussion

Structures resolution and description

XRD data collections were carried out on selected orange (with different shade of orange color depending on the O/S ratio) or red single crystals found in the different preparations in which the targeting compositions were $Ba_5(VO_3S)_3X$ (X= F, Cl, I). Compositions targeting (VO_2S_2) for the O/S ratio around vanadium will be discussed later in the "powder" section. Three single crystals from

different preparations with X= Cl were studied and their structures solved in the hexagonal symmetry in space group $P6_3/mcm$ (193). Surprisingly, they yield slightly different O/S ratio in the range of the targeted one. In comparison, the oxide reported analogue $Ba_5(VO_4)_3Cl$ crystallizes in the less symmetric $P6_3/m$ space group. For our sulfur substitued Cl-based crystals (C1, C2 and C3), additional weak intensity spots were detected in the precession images. The analysis of the single crystal XRD data showed that the later do not correspond to a modulation or a superstructure. Instead, they are due to tiny crystals stuck on the main crystal. Since their relative proportion is estimated to be less than 5%, they were not considered in the refinement, knowing that no systematic superposition was observed with the main crystal. Here, we observe that the incorporation of sulfur impacts the symmetry although the apatite type is preserved. The main differences between the three Chloride-based crystals are listed in Table 1. For clarity, those crystals are called c1, c2 and c3 with sulfur content increasing from c1 to c3. Their data collection and refinement details are given in Table 2. The treatment of the data was performed with Jana2006[15] and charge flipping[16] for structural solution and least squares method for refinement. The examination of the precession images constructed in the 0kl,h0l and hk0 planes (Figure S1) are consistent with our unit cell choice. As already evoked, they also exhibit weak additional reflections that we were attributed to a small crystal of the same phase stuck on the main one, which did not hamper high quality refinements.

The common structure type of the three phases within this new family $Ba_5(VO_{4-\alpha}S_\alpha)_3Cl$, belongs to the well-known halide-apatite type with general formula $M_5(M'O_4)_3X$ (M = divalent cation such as an alkaline earth, Pb^{2+} etc…, M' = pentavalent cation, and X = F, Cl, Br or OH). The later is constituted by disconnected vanadate groups separated by Ba^{2+} cations and delimiting channels occupied by halide anions. In the new series we present here, the vanadate groups are replaced by thiovanadates ($VO_{4-\alpha}S_\alpha$) which exhibit O/S mixed environment (also called heteroleptic) around V^{5+}. The unit cell represented in projection (001) is shown in Figure 1.a. The Ba^{2+} cations are located in two different crystallographic sites (4d and 12k), while Vanadium atoms are defined with only one site (4d). There are two distinct anionic sites coordinating V^{5+}. The 12k O1(S1) is disordered with mixed O/S occupancy while O2 (12j) is fully occupied by oxygen. Depending on the O/S ratio, a possible splitting of Ba2 and Cl1 atoms into two positions is observed. When

Sulfur content increase, the mean V1-(O1/S1), and Ba2-(O1/S1) distances slightly increases (as well as the volume of the unit cell) accordingly, as expected from the greater S^{2-} ionic radii. During the refinement, the large anisotropic elongation of the thermal parameter of Cl within the channel was such that a split position (into two half-occupied 4e sites) was required to better describe the two lower oxygen compositions. For the highest ratio O/S found (α=0.966) both atoms Ba2 and Cl1 are also splitted into two positions. Then for crystal c2, when O/S decrease, only Cl1 is split.For c3 with lowest O/S ratio, no split position was observed, but the reliability factor slightly increased.

Taking the case of α=1.437 with greater sulfur incorporation (no split positions), Ba2 is coordinated to two Cl, two O1/S1 and two S2 atoms. In the case of α=1.123, the split Cl lead to the $d_{Ba2-Cl1}$=3.09(2) Å (x2) distances with no Ba2 split. For α=0.966, Cl is split into two positions as well as Ba2. The trend is clearly that when the sulfur content increases, the average structure within $P6_3/mcm$ space group become more and more ordered (less split and disordered sites). However, the reliability factors are slightly increasing. In C3, the most ordered case, the halide anions are coordinated by six Baryum atoms (**Figure 1.b**) with d_{Ba-Cl}=3.392(2) Å. This value is slightly longer than that found in $Ba_5(VO_4)_3Cl^{17}$ d_{Ba-Cl} = 3.288(1) Å. Shorter distance is found in C2 where Cl is split into two positions d_{Ba-Cl} =3.09(2)x2 Å. In the thiovanadate species $VO_{4-\alpha}S_\alpha$ (Figure 1.c) d_{V-O} ranges from 1.688(7) to 1.696(112) Å. These values are in the same range than other thiovanadate compounds (for instance d_{V-O}= 1.68 Å in $Ba_5(VO_2S_2)_2(S_2)_2^9$ and d_{V-O}= 1.626 Å, in $Ba_{15}V_{12}S_{34}O_3^{18}$). For the disordered site O/S, $d_{V-(O/S)}$ was found between 2.001(3) and 2.046(7) Å. The distance is directly related to the O/S ratio and its value lying between the value expected for V^{5+}-O and the one expected for V^{5+}-S. Ba1 atom is exclusively coordinated to oxygen atoms to form a regular BaO_6 octahedra with six Ba–O of 2.841(7) Å. Cell parameters and volume evolution with variation of sulfur percentage are plotted in Figure 2. Atomic Positions and Isotropic Thermal Displacements, Anisotropic Thermal Parameters Uij (Å^2) and main distances for C1, C2 and C3 are listed in Table 3, Table S2 and Table4, respectively. EDS analysis results carried out on several Chloride-crystals show good agreement between the theoretical ratios and EDS ratios (Table S1).

For the fluorine-crystal, we index a unit cell corresponding to a superstructure of the oxide $Ba_5(VO_4)_3F$. The structure could besolved and refined in a trigonal symmetry in space group P-

3m1 (164) and is still related to the apatite type. Note here that several different space groups were tested but finally ruled out because of strong residual electron density problems, higher reliability factors and, *in fine*, no justification for the non-centrosymmetry. More into details of the structure, the only disorder within the structure is observed for some Ba atoms. Three of the five Ba locations (Ba1, Ba4 and Ba5) are disordered with an additional close position with complementary occupancy (Ba1a, Ba4a and Ba5a, respectively). Fluoride atoms occupy four different crystallographic sites into two types of channels. F1 and F2 are partially filled with complementary occupation to avoid their too short distance. The Ba-F distances are in the range 2.554(6)-2.605(8) Å, in good agreement with those observed in $Ba_5(VO_4)_3F$[19] with d_{Ba-F} =2.489(16) and 2.768(68) Å. The heteroleptic VO_3S tetrahedra are here fully ordered with no mixed O/S sites and with distances d_{V-S} ranging from 2.081(8) to 2.198(7)Å and d_{V-O} distances ranging from 1.694(15) to 1.909(10) Å.

A red single crystal for *X*= I⁻ could also be isolated and single crystal diffraction collected. The same unit cell is found as in the Fluorine case just described and the structure could be solved in the same space group *P*-3m1 with a=18.4866(10) Å and c=8.6695(9) Å. However, at this stage a complex disorder within the channels needs to be treated which requires improved crystal quality. We will not discuss this phase in detail as it is still under progress.
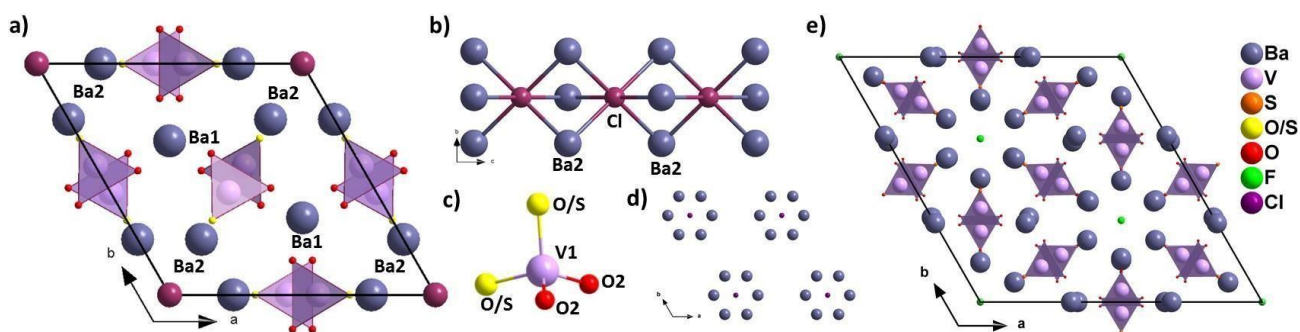

Figure 1. a) Thio-apatite unit cell projected along c-axis for the most ordered phase $Ba_5V_3O_{7.869}S_{4.131}Cl$. b) Cl environment: $ClBa_6$ connected polyhedra. c) Disordered thio-vanadate tetrahedra $VO_2(O/S)_2$. d) View of channels occupied by chloride anion. e) Superstructure unit-cell of $Ba_5V_3O_9S_3F$ projected along c- axis.

Table 1. Main refinement data for the reported phase $Ba_5V_3O_{12}Cl$ and the three single crystals of Chloro-thio-apatites C1, C2 and C3.

	Formula	Cell parameters (Å)	Space group	R_{obs}	Volume (Å)	Split positions

	$Ba_5V_3O_{12}Cl$ [ref. 17]	a=10.5565(1) c= 7.7584(1)	$P6_3/m$	1.50 [ref. 17]	748.76(14)	*none*
C1	$Ba_5V_3O_{9.102}S_{2.898}Cl$	a=10.6048(3) c= 8.6962(5)	$P6_3/mcm$	3.98	846.96(6)	Ba2 Cl1
C2	$Ba_5V_3O_{8.632}S_{3.368}Cl$	a= 10.5913(9) c= 8.8891(16)	$P6_3/mcm$	5.75	863.55(19)	Cl1
C3	$Ba_5V_3O_{7.869}S_{4.131}Cl$	a= 10.5935(3) c= 8.9630(7)	$P6_3/mcm$	6.79	871.09(8)	*none*
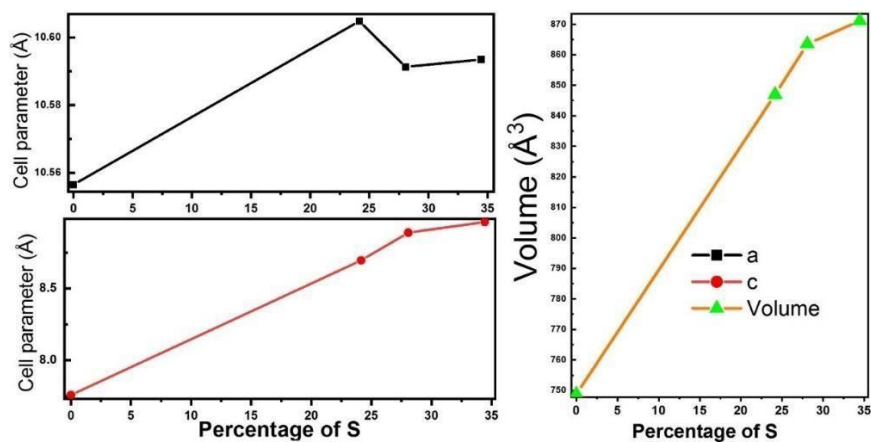
Figure 2. Cell parameters and volume evolution with O/S ratio variation for $Ba_5(VO_{4-\alpha}S_\alpha)Cl$ based on the single crystal data.

Table 2. Data Collection and Refinement Details for the chloride-based crystals C1, C2 and C3 and the fluoride-based crystal C4.

Crystal	C1	C2	C3	C4
Formula	$Ba_5V_3O_{9.102}S_{2.898}Cl$	$Ba_5V_3O_{8.552}S_{3.448}Cl$	$Ba_5V_3O_{7.869}S_{4.131}Cl$	$Ba_5V_3O_9S_3F$
Detailed formula $Ba_5(VO_{4-\delta}S_\delta)_3Cl$				
$\delta=$	0.966	1.123	1.437	1
Molecular weight (g. mol^{-1})	1113.5	1121.1	1133.3	1098.7
Symmetry		*Hexagonal*		
Space group	$P6_3/mcm$ (193)	$P6_3/mcm$ (193)	$P6_3/mcm$ (193)	$P\bar{3}m1$ (164)
Unit cell dimensions (Å)	a= 10.6048(3)	a=10.5913(9)	a= 10.5935(3)	a= 18.1597(8)
	c= 8.6962(5)	c= 8.8891(16)	c= 8.9630(7)	c= 8.8299(5)
Volume (Å^3)	846.96(6)	863.55(19)	871.09(8)	2521.8(2)
Z	2	2	2	6
Data Collection				
Equipment		Bruker X8 Apex 4K		
Wavelenght [Å]	0.56087 (Ag)	0.56087	0.56087	0.71075 (Mo)
Calculated density (g cm^{-3})	4.3662	4.3114	4.3208	4.3408
Crystal shape	Platelet	Platelet	Platelet	Platelet
Crystal dimensions (μm)	45×25×5	35×22×5	68×38×6	50×40×5
Color	Orange	Orange	Orange	orange
Absorption correction	Analytical	Analytical	Analytical	Multi-Scan
Scan mode	ω, φ	ω, φ	ω, φ	ω, φ
θ (min–max) (°)	1.75- 24.4	1.75-18.31	1.75-22.5	2.24 - 26.01
Calculated μ (mm^{-1})	7.129	7.019	7.002	13.512
F(000)	970	979	990	2868
Reciprocal space recording	$-15 \leq h \leq 14$ $-14 \leq k \leq 15$ $-12 \leq l \leq 12$	$-11 \leq h \leq 11$ $-11 \leq k \leq 11$ $-9 \leq l \leq 9$	$-14 \leq h \leq 14$ $-14 \leq k \leq 14$ $-12 \leq l \leq 12$	$-22 \leq h \leq 22$ $-22 \leq k \leq 22$ $-10 \leq l \leq 10$
No. of measured reflections	42508	33181	45845	37203
No. of independent reflections	545	256	451	1828
I > 3σ(I) (total)	394	223	302	1370
Refinement details				
Number of refined parameters	29	27	26	98
Refinement method	Least-squares	Least-squares	Least-squares	Least-squares
Weighting scheme	sigma	sigma	sigma	sigma
R1(F) [I > 3σ(I)]/R1(F^2) (all data, %)	0.0398/0.0592	0.0575/0.0673	0.0679/0.0965	0.0588 /0.0781

wR2(F²) [I > 3σ(I)]/wR2(F²) (all data, %)	0.0452/0.0501	0.0692/0.0708	0.0794/0.0823	0.0748 /0.0769
Goodness of Fit	2.69	4.25	3.45	3.19
Max/Min residual electronic density ($e^-/Å^3$)	1.34/-1.37	2.61/-2.44	5.36/-5.31	4.09 / -2.78
T_{min}/T_{max}	0.6916/0.7451	0.6154/0.7442	0.6118/0.7448	0.6365/ 0.7453

Table 3. Atomic Positions and Equivalent Thermal Displacement for C1, C2 and C3 respectively.

Atom	Wyck.	s.o.f.	x	y	z	U_{eq}
C1-Ba$_5$V$_3$O$_{9.102}$S$_{2.898}$Cl						
Ba1	4d	1	0.666667	0.333333	1	0.0435(3)
Ba2	12k	0.5	0.2448(1)	0.2448(1)	0.7077(1)	0.0336(3)
V1	6g	1	0.5628(2)	0.5628(2)	0.75	0.0460(8)
Cl1	4e	0.5	0	0	0.5689(11)	0.052(2)
O1	12k	0.52(2)	0.3180(3)	0.3180(3)	0.4283(4)	0.050(2)
S1	12k	0.48(2)	0.3180(3)	0.3180(3)	0.4283(4)	0.050(2)
O2	12j	1	0.5388(6)	0.3930(6)	0.75	0.051(3)
C2-Ba$_5$V$_3$O$_{8.552}$S$_{3.448}$Cl						
Ba1	4d	1	0.666667	0.333333	0	0.0447(9)
Ba2	6g	1	0.7583(2)	0.7583(2)	0.25	0.090(1)
V1	6g	1	0.4400(5)	0.4400(5)	0.25	0.050(2)
Cl1	4e	0.5	0	0	-1.444(4)	0.10(2)
O1	12k	0.43(5)	0.3207(7)	0.3207(7)	0.4291(11)	0.054(4)
S1	12k	0.57(5)	0.3207(7)	0.3207(7)	0.4291(11)	0.054(4)
O2	12j	1	0.5388(6)	0.3930(6)	0.75	0.051(3)
C3-Ba$_5$V$_3$O$_{7.869}$S$_{4.131}$Cl						
Ba1	4d	1	0.666667	0.333333	0	0.0396(7)
Ba2	6g	1	0.7597(2)	0.7597(2)	0.25	0.078(1)
V1	6g	1	0.4420(4)	0.4420(4)	0.25	0.046(2)
Cl1	2b	1	0	0	0	0.157(14)
O1	12k	0.31(5)	0.3220(6)	0.3220(6)	0.0712(9)	0.057(3)
S1	12k	0.69(5)	0.3220(6)	0.3220(6)	0.0712(9)	0.057(3)
O2	12j	1	0.6118(13)	0.4640(13)	0.25	0.049(6)

Table 4. Selected interatomic distances (Å) for C1, C2 and C3.

Atoms 1,2	d 1,2 [Å]	Atoms 1,2	d 1,2 [Å]
	C1-$Ba_5V_3O_{9.102}S_{2.898}$ Cl		
Ba1-O2	2.797(5)x6	Ba2-Cl1	3.242(5)
Ba2-O1/S1	2.551(3)x2	Ba2-O2	2.725(5)x2
Ba2-O1/S1	3.259(4)	V1-O1/S1	2.001(3)x2
Ba2-O1/S1	3.280(5)x2	V1-O2	1.688(7)x2
Ba2-Cl1	2.863(4)	Cl1-Cl1	1.200(12)
	C2-$Ba_5V_3O_{8.552}S_{3.448}$Cl		
Ba1-O2	2.829(14)x6	Ba2-O2	2.718(18)x2
Ba2-O1/S1	2.974(9)x2	V1-O1/S1	2.032(8)x2
Ba2-O2	2.718(18)x2	V1-O2	1.69(2)x2
Ba2-Cl1	3.09(2)x2	Cl1-Cl1	1.00(5)
	C3-$Ba_5V_3O_{7.869}S_{4.131}$Cl		
Ba1-O2	2.841(7)x6	Ba2-O2	2.713(9)x2
Ba2-O1/S1	3.006(8)x2	V1-O1/S1	2.046(7)x2
Ba2-O2	2.713(9)x2	V1-O2	1.696(12)x2
Ba2-Cl1	3.392(2)x2		

Table 5. Atomic Positions and Equivalent Thermal Displacement for C4, Ba_5 $(VO_3S)_3$ F

			C4-$Ba_5V_3O_9S_3F$			
Atom	Wyck.	s.o.f.	x	y	z	U_{eq}
Ba1	6i	0.88(2)	0.58523(6)	0.41477(6)	0.2059(7)	0.0209(9)
Ba1a	6i	0.12(2)	0.5897(5)	0.4103(5)	0.268(4)	0.019(4)
Ba2	6g	1	0.67810(7)	0.67810(7)	0	0.0352(5)
Ba3	6h	1	0.65546(7)	0.65546(7)	0.5	0.0360(5)
Ba4	6i	0.773(8)	0.91881(4)	0.83763(9)	0.2900(4)	0.0235(8)
Ba4a	6i	0.227(8)	0.91975(16)	0.8395(3)	0.2047(12)	0.0202(19)
Ba5	6i	0.664(9)	0.49536(10)	0.74768(5)	0.2930(5)	0.0229(10)
Ba5a	6i	0.336(9)	0.4950(2)	0.74750(12)	0.2120(9)	0.0222(13)
V1	6i	1	0.47615(9)	0.52385(9)	0.2250(4)	0.0242(12)
V2	6i	1	0.71386(19)	0.85693(10)	0.2708(4)	0.0297(12)
V3	6i	1	0.80965(10)	0.6193(2)	0.2570(5)	0.0425(15)
S1	6i	1	0.1226(3)	0.56129(17)	0.4352(6)	0.0359(13)
S2	6i	1	0.10369(19)	0.2074(4)	0.0748(7)	0.0437(14)
S3	6i	1	0.7735(2)	0.5470(4)	0.0596(8)	0.0523(16)
O1	12j	1	0.5832(6)	0.5662(6)	0.2232(10)	0.030(2)
O2	12j	1	0.7691(6)	0.6853(7)	0.2624(12)	0.044(3)
O3	12j	1	0.6480(6)	0.7500(6)	0.2691(11)	0.038(2)
O4	6i	1	0.7688(3)	0.5375(6)	0.4168(11)	0.007(2)
O5	6i	1	0.7872(8)	0.8936(4)	0.4390(15)	0.028(3)
O6	6i	1	0.4370(5)	0.5630(5)	0.0809(18)	0.047(4)
F1	2c	0.81(2)	1	1	0.278(3)	0.039(6)
F2	1b	0.37(5)	1	1	0.25	0.039(6)
F3	2d	1	0.666667	0.333333	0.218(4)	0.077(12)
F4	2d	1	0.333333	0.666667	0.239(5)	0.108(16)

Table 6. Selected interatomic distances (Å) for C4.

Atoms 1,2	d 1,2 [Å]	Atoms 1,2	d 1,2 [Å]
Ba1-S1	3.258(9)	Ba5-S3	3.218(8)
Ba1-S3	3.304(5)x2	Ba5-O3	2.759(13)x2
Ba1-O1	2.772(12)x2	Ba5-O4	2.647(11)
Ba1-O6	2.627(17)	Ba5-F4	2.592(8)
Ba1-F3	2.564(2)	Ba5a-S3	2.534(10)
Ba2-O1	2.735(8)x2	Ba5a-O3	2.802(13)x2
Ba2-O2	2.810(11)x2	Ba5a-F4	2.554(6)
Ba3-O1	2.863(9)x2	V1—S1	2.198(7)
Ba3-O2	2.799(11)x2	V1—O1	1.696(10)x2
Ba3-O3	2.712(11)x2	V1-O6	1.770(14)
Ba4-S2	3.299(7)	V2-S2	2.128(7)
Ba4-O2	2.754(8)x2	V2-O3	1.697(9)x2
Ba4-O5	2.521(13)	V2-O5	1.880(13)
Ba4-F1	2.5559(18)	V3-S3	2.081(8)
Ba4a-S2	3.177(10)x2	V3-O2	1.694(15)x2
Ba4a-S2	2.576(12)	V3-O4	1.909(10)
Ba4a-O2	2.815(9)x2		
Ba4a-F1	2.605(8)		
Ba5-S1	3.257(7)x2		
Ba5-S3	3.218(8)		

Polycrystalline Phase Analysis

Here it is important to distinguish the compositions (ratio O/S in the thiovanadates) refined from single crystals and the one obtained in the case of powders. All initial synthesis (including in the preparations where single crystals were selected) were formulated considering simple O/S ratios within thiovanadates to target VO_3S and VO_2S_2 in a first step. (VS_3O and higher sulfur content are still under investigation).

The synthesis of pure powder samples in those systems were carried out following the procedure described in the Experimental Section. For Fluorine, Chlorine and Iodide-phases, we attempted the synthesis starting from simple O/S ratios corresponding to either VO_3S or VO_2S_2 tetrahedra. At this stage, we could not reach a powder sample of an iodide-phase as major phase (although we could clearly identify such a phase in the products) and thus we present results for F and Cl only, i.e. with the nominal compositions $Ba_5(VO_3S)_3F$, $Ba_5(VO_2S_2)_3F$, $Ba_5(VO_3S)Cl$ and $Ba_5(VO_2S_2)_3Cl$. For clarity, nomenclature phase 1, phase 2, phase 3 and phase 4 were attributed to them, respectively. Phases 1, 2 and 3 are obtained pure or almost pure (few weak impurity peaks are observed in some preparations) as shown in Figure 3, while for phase 4, the minor impurity $Ba_6(VO_2S_2)_2(VS_3O)(VS_4)$ (*i.e.* $Ba_6V_4S_{11}O_5$) was clearly identified and taken in account in the PXRD refinement. Figure 3 shows the Le bail fit for the four powders obtained from the above-mentioned compositions using Jana2006 software. In the case of the Fluorine-phase

1, the profile refinement of the XRD patterns confirms that the super-structure observed in the single crystal Fluorine-phase is relevant. For simplicity at this stage of the work, we present profile refinement and we assume, regarding the unit cells refined and the purity, that the powders have compositions close to the targeted ones. For phase 1, $Ba_5(VO_3S)_3F$, we find a= 18.1655(4) Å and c= 8.8482(3) Å in P-$3m1$ which is very close to the unit cell parameters refined for the single crystal of the same composition. To improve the profile refinement, we considered a symmetry lowering toward the monoclinic symmetry which allowed the better modelling of a particular peak as detailed in S2. However, we do not consider it further in this work because of the small effect and of the the single crystals results. In addition, it would require additional diffraction experiments with complementary tools to validate or not.

For phase 2 to 4, the unit cell in $P6_3/mcm$ was used as foundfrom the Chloride-single crystals. For phase 2, $Ba_5(VO_2S_2)_3F$, a=10.4903(1) Å and c=9.4956(1) Å. For phase3, $Ba_5(VO_3S)Cl$, a= 10.6612(2) Å and c= 8.6356(2) Å. For phase 4, $Ba_5(VO_2S_2)_3Cl$, a= 10.6264(2) Å and c=8.9906(3) Å. From phase 3 to 4, we observe that a parameter is slightly decreasing while the c parameter is significantly increasing with overall an increase of the volume (from V= 850.03(4) Å^3 to V= 879.21(4) Å^3). This increase of the volume in the Cl-phases from phase 3 to 4 is consistent with the greater sulfur content in phase 4. Comparing with single crystal data, these unit cell parameters are consistent, since we observe little change in the a parameter and an evolution mostly on the c parameter. Powder phase 3 has unit cell parameters consistent with C1 crystal with a close composition (table 2). Besides, phase 4 is closest to the C3 crystal (table 2) but with a higher expected sulfur content which agrees with its greater unit cell volume. Here in powder of phase 4, we should keep on mind the significant presence of the impurity $Ba_6V_4S_{11}O_5$ which may indicate a deviation from the targeted composition. On another hand, from the F-phase 2 and the Cl-phase 4 (with expected similar O/S ratio), the unit cell parameters increase from F to Cl consistently with their respective ionic radii.
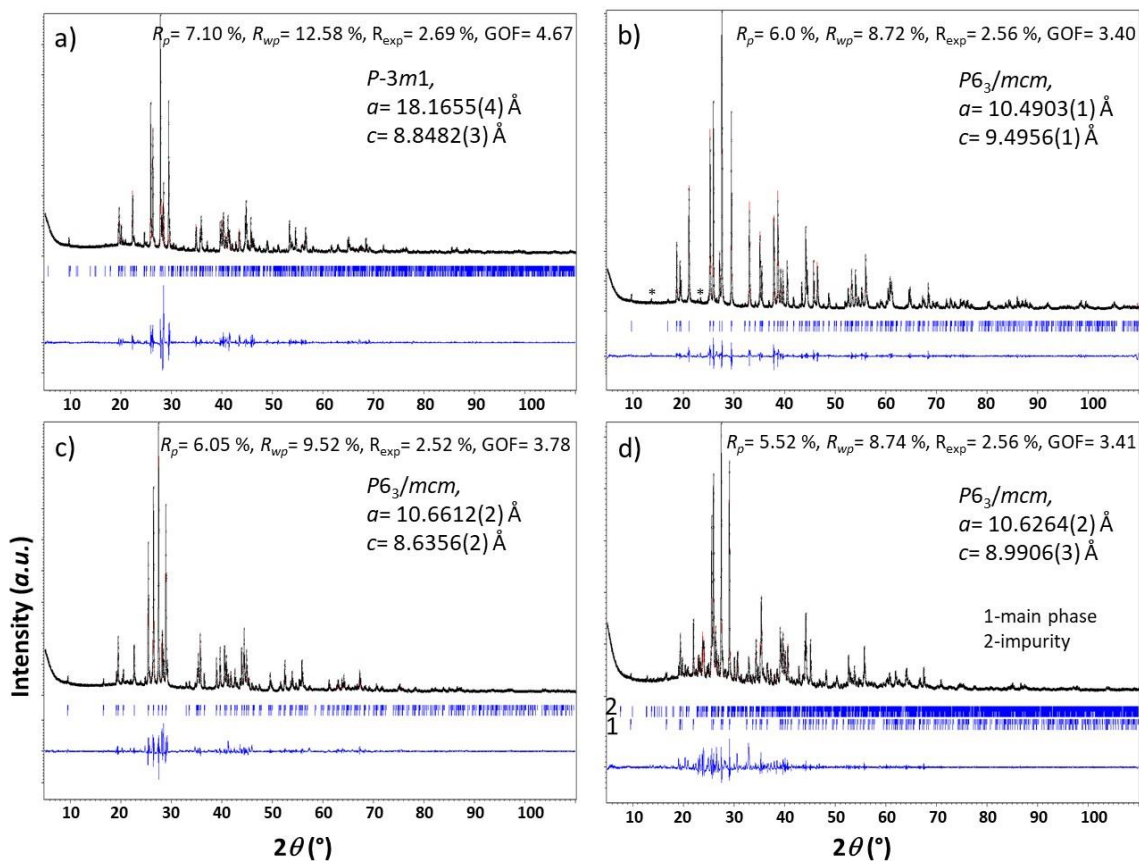
Figure 3. a) to d) PXRD profile refinement of phases 1 → 4. (a) to (d) correspond to phase 1 to 4, respectively, *i.e.* (a) $Ba_5(VO_3S)_3F$, (b) $Ba_5(VO_2S_2)_3F$, (c) $Ba_5(VO_3S)Cl$ and (d) $Ba_5(VO_2S_2)_3Cl$. Reliability factors and refined unit cell parameters are indicated on the graphs. Few impurity peaks are indicated by a star. Experimental and calculated diagrams are superimposed and respectively represented in black and red. Bragg peaks positions and difference between calculated and simulated diagrams are represented in blue.

Optical Measurements and DFT calculations

The UV–visible diffuse-reflectance analysis of the polycrystalline phases is represented in Figure 4. A Kubelka–Munk[20] transformation was applied to the measured diffuse- reflectance (R) spectrausing the function F(R) = (1 − R)²/2R. Then a Tauc plot[21,22] was used to determine the optical bandgap E_g, using the equation $[F(R) hv]^{1/n} = k(hv − E_g)$, where hv is the photon energy, k an energy- independent constant, E_g the optical band gap, and n is an exponent related to the type of transition. Assuming an indirect transition (exponent n = 2), the plot of $[F(R) hv]^2$ *versus* hv leadsto E_g in the range 2.11 − 2.48 eV, thus in the visible range. We note here however that the contribution of the impurity in phase 4 may hamper the exact determination of the band gap. Comparatively the oxyhalide based on vanadate groups

16

$Ba_5(VO_4)_3F$ was reported with a bandgap in the UV range (E_g= 3.85 eV). We confirm here the expected drastic shift of the band gap in the visible range upon sulfur incorporation contained in the thiovanadate species. More into details, the band gaps are reduced from phase 1 to 2 and from phase 3 to 4 consistently with thegreater sulfur content of lower electronegativity from VO_3S to VO_2S_2 units. Then, considering similar O/S ratio, the band gap is reduced from phase 1 to 3 and from phase 2 to 4, when the halide is changed from F to Cl consistently with the lower electronegativity of Cl. Here we show how finely we can tune the band gap with such a versatile structure that can accommodate O^{2-}, S^{2-}, F^- and Cl^- (and I^- not discussed here) with various O/S ratios.
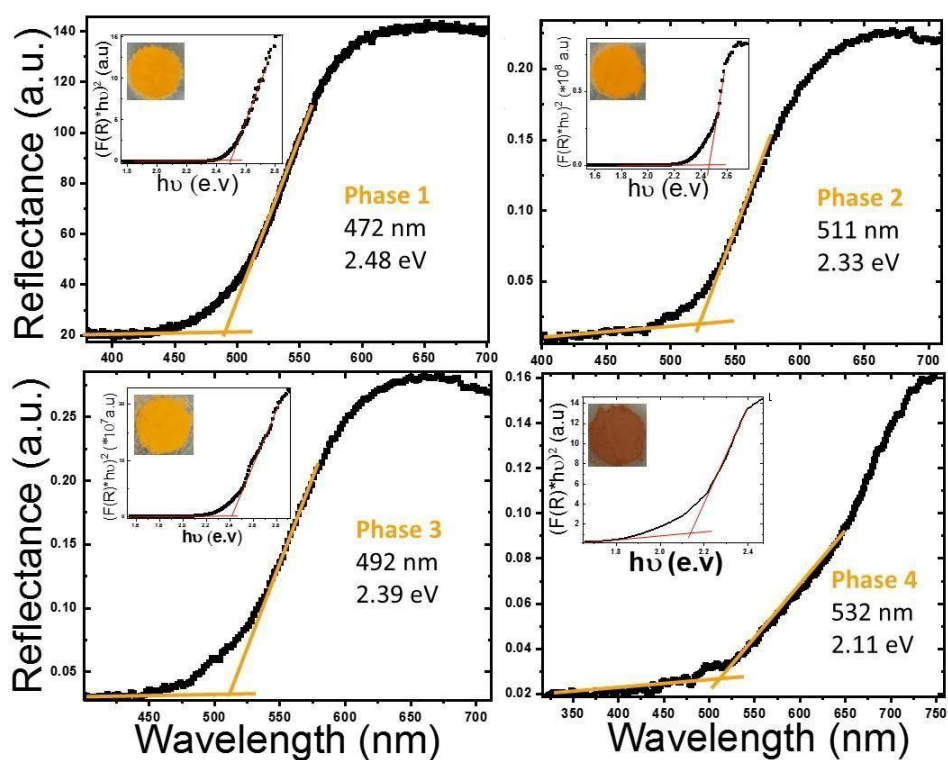
Figure 4. Diffuse-reflectance spectra for phases 1 →4 successively with a Tauc plot as insets to determine the experimental band gap.

Our DFT calculated total density of states for $Ba_5(VO_4)_3Cl$, $Ba_5(VO_4)_3F$, $Ba_5(VO_3S)_3Cl$, $Ba_5(VO_3S)_3F$ are depicted in Figure 6, which were calculated using simplified (fully ordered) optimized structural models. Values of the band gaps are also indicated in the inset of the figures. Our theoretically calculated values of band gaps are 4.15 eV, 4.18 eV, 2.49 eV, 2.53 eV for $Ba_5(VO_4)_3Cl$, $Ba_5(VO_4)_3F$, $Ba_5(VO_3S)_3Cl$, $Ba_5(VO_3S)_3F$ respectively. It is very clear from the electronic structure calculated, that

a S doping in O sites reduces the band gap in both $Ba_5(VO_4)_3Cl$, $Ba_5(VO_4)_3F$ compounds and that band gaps lie in the visible-light range (Figure 5, Figures S3, S4 and S5). Note that our calculated band gaps for $Ba_5(VO_3S)_3Cl$, $Ba_5(VO_3S)_3F$ systems are consistent with our experimental results. We also calculate the atom projected density of states for all these above-mentioned systems as depicted in Figure 5. Electronic states just below Fermi levels are dominated by O and S p-orbitals whereas conduction bands are dominated by V d-orbitals as well as Ba d-orbitals. It is also quite evident that S states are arising significantly at the top of the valence band in $Ba_5(VO_3S)_3Cl$, $Ba_5(VO_3S)_3F$. We also observe that with the S doping in O sites, halide (Cl/F) states are shifted away from the Fermi level. We also present calculated band structures and density of states of $Ba_5(VO_4)_3Cl$ and $Ba_5(VO_3S)_3Cl$ in Figure S3-S4 in order to see the effect of S substitution in O sites. Finally, in order to see the effect of increasing S/O ratio we calculate density of states for $Ba_5V_3O_8S_4Cl$ (Figure S5). Clearly, with increasing S doping a band gap decrease is calculated, which is also observed in our experiments.
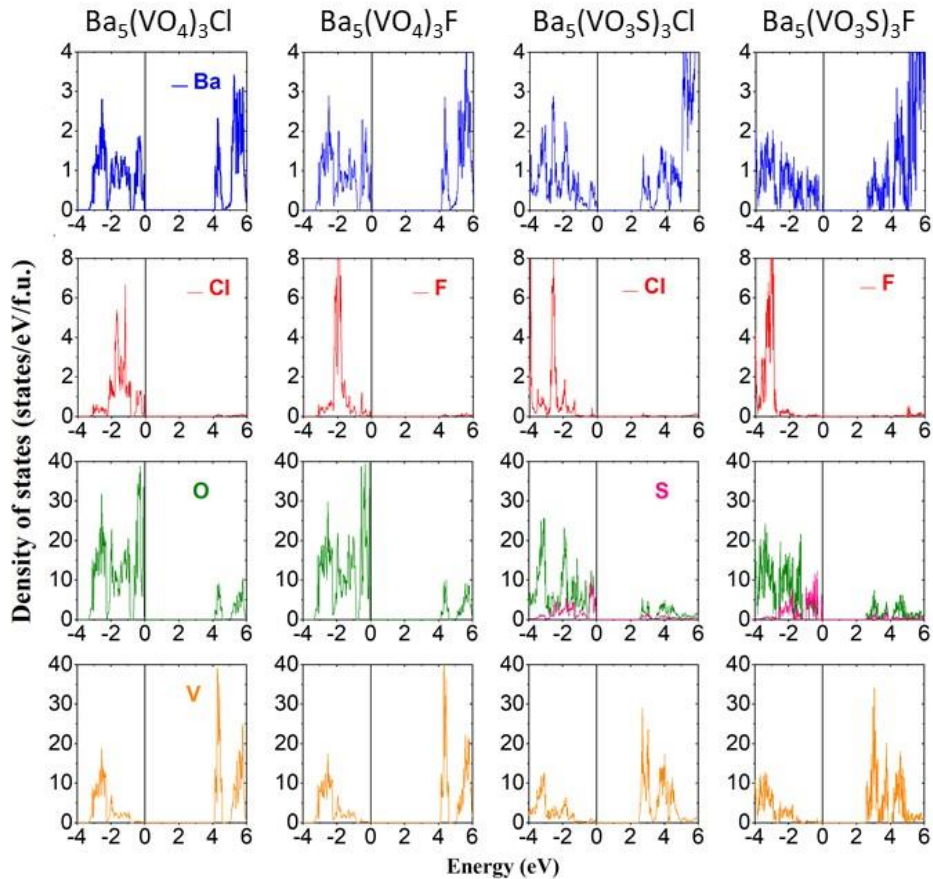

Figure 5. Calculated atom projected density of states of $Ba_5(VO_4)_3Cl$, $Ba_5(VO_4)_3F$, $Ba_5(VO_3S)_3Cl$ (C3), and $Ba_5(VO_3S)_3F$ (C1).

Photoactivated Transport

Mott-Schottky (MS) measurements ($1/C^2$ *vs.* V) were performed to elucidate the flat-band potential (V_{fb}) and to determine the type of semiconductor of all powder phases of $Ba_5 (VO_{4-\alpha}S_\alpha)_3X$. MS plots shows a positive slope (Figure 6.b) which indicate *n*-type semiconductors where the majority charge carriers are electrons. The flat-band potentials for powders 1, 2, 3 and 4 were estimated to be approximately -0.62, -0.31, -0.55 and -0.27 V vs. Ag/AgCl, respectively. This potential allows locating the conduction band edge assuming that V_{fb} is lower by 0.1–0.3 V from the conduction band for *n*-type semiconductors[23]. It is clear that the valence band maximum (VBM) shifts negatively from X= F to the less electronegative X=Cl (χ_F= 3.98 and χ_{Cl}= 3.16) and by increasing S/O ratio (χ_O= 3.44 and χ_S= 2.58).

This is also consistent with the alignment of the bands shown in Figure 6.a. We have calculated the laterfrom empirical calculations based on Mulliken electronegativities as proposed by Butler and Ginley[24] and as further described by Xu and Schoonen[25]. Castelli *et al.*[26] have performed such calculations for a large set of materials including mixed anion oxynitrides and analysed how they align with the levels for hydrogen and oxygen evolution. In our case, the band edges positions encompass the redox potential of water which is required to evolve hydrogen and oxygen. Therefore, as shown from the comparison of the vanadate $Ba_5V_3O_{12}F$, the incorporation of thiovanadates preserve suitable band alignments for water-splitting reaction while it allows to shift the band gap in the visible range. Moreover, the samples having lower slopes indicate higher electron concentration in the crystal. However, the density of charge carriers cannot be estimated without knowing the effective dielectric constant of the mixture consisting of the phase analyzed and the polymer.
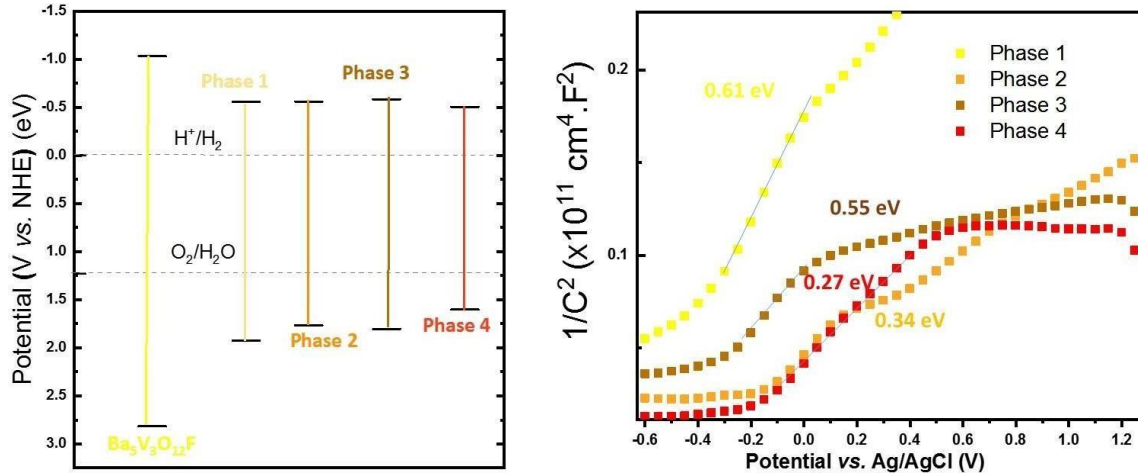
Figure 6. a) Calculated band edges positions obtained from empirical calculations for $Ba_5V_3O_{12}F$ and phases 1,2,3 and 4 respectively. The levels for hydrogen and oxygen evolution are indicated by dashed lines. b) Mott-Schottky plots carried out on the powders deposited on a slide of ITO/glass.
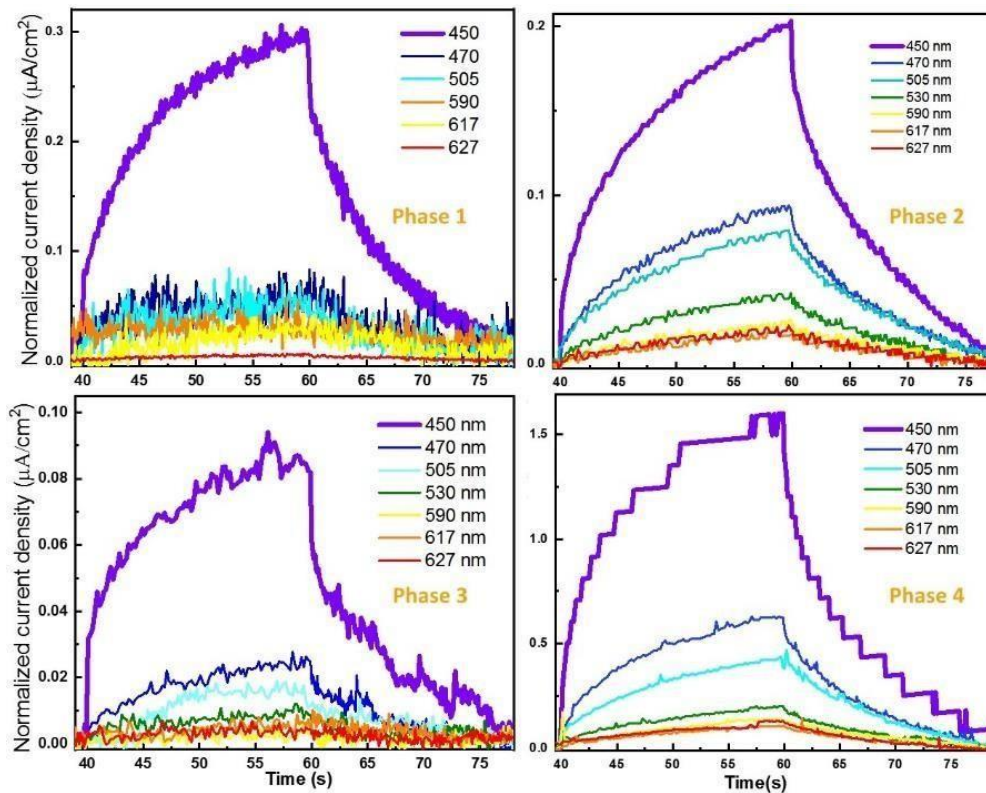
Figure 7. Evolution of the transient photo-current response for various wavelengths (performed under a constant luminous flux density of 42 mW.cm^{-2} on a film deposited on a ITO/glass substrate.

Figure 7 shows the influence of wavelengths on the transient photocurrent response. The photocurrent density (Δj) increases when the wavelength decreases for all samples. Samples 1 and 3 show a sharp drop between 450 and 470 nm showing an abrupt evolution in material absorption, while samples 2 and 4 show a gradual attenuation with increasing wavelength. Knowing that the photocurrent generated is proportional to the absorbance of the material. This change is also observed on the reflectance spectra. In **Figure 7**, a maximum variation of the photo-current density occurring under an excitation of 450 nm is observed and prove the generation of a photocurrent of about 0.1, 0.2, 0.3 and 1.5 μA/cm^2 for phase 1 to 4, respectively under 42 mW.cm^{-2}. The fact that phase 4 has a value one order of magnitude higher than the others has to be further investigated because there is probably a higher transfer rate compared to the recombination rate but could also be related to the presence of the impurity $Ba_6(VO_2S_2)_2(VS_3O)(VS_4)$.
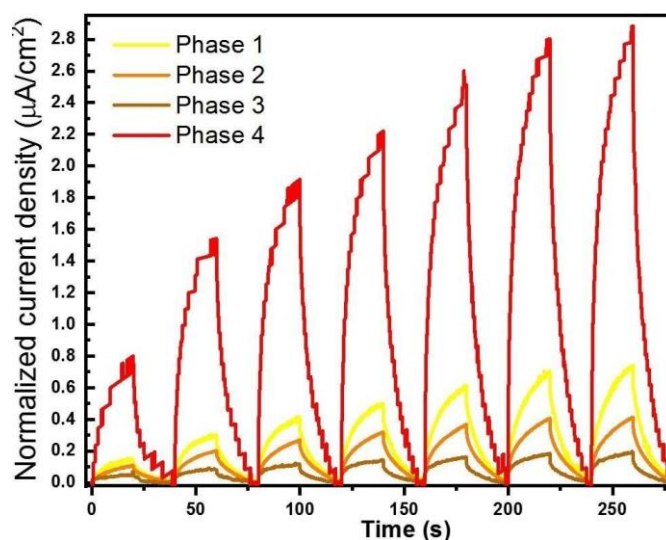
Figure 8. Variation of normalized current density *under increasing intensity illumination* (450 nm) or in the dark and with an applied potential of 0.2 V vs Ag/AgCl.

The on/off variation at 450 nm is maximal and present a photocurrent density of 0.8, 0.4, 0.2 and 2.8 μA.cm^{-2} for phases 1, 2, 3 and 4, respectively with a bias potential of 0.2 V *vs* Ag/AgCl and under a light intensity (φ_0) of more mW.cm^{-2}. The evolution of the photocurrent Δj with the intensity of the luminous flux (λ = 450 nm; V = 0.2 V *vs* Ag/AgCl) is shown in Figure 8. The photocurrent density variation follows, in some cases, a power-type law whosemodel data are presented in Table 7 and Figure 9.

For phase 1, the evolution of the current density ($\Delta j = j_{light} - j_{dark}$) follows a quasi-linear evolution with γ close to 1. For the other phases, a power law evolution is clearly demonstrated. For low intensities, the generated photocurrent is directly proportional to the light intensity. The electron-hole pairs created are mainly transferred to the surface towards the electrode. Beyond a certain limit value of luminous intensity, the dependence is carried out in square root. This evolution of the exponent is probably not translated by a limitation of the charge transfer and a higher rate of recombination of the electron-hole pairs. This point is widely described in photocatalysis, in particular to explain a nonlinear evolution in the dyes photodegradation as a function of the luminous flux[27,28]. In this case, the limit between the two modes is depending on

22

the level of impurities compared to the density of the photoelectrons. This non-integer exponent can be regarded as a consequence of a complex process of electron–hole generation, trapping and recombination in the semiconductor[29]. Ullrich *et al.*[30] present a quantitative explanation to non-linearities phenomena. If we neglect the diffusion of carrier, the equilibrium between carrier generation and recombination is expressed by the following equation:

$$G = Bn\ (n+M) \propto \phi_0$$

Where G is the generation rate of photoelectrons by incident light (directly proportional to the luminous intensity); B is the recombination coefficient; n is the density of photoelectrons (whose value is proportional to the intensity of photocurrent) and M is the number of impurity levels per cm^3.

At low intensities or for high impurity concentrations (n<<M), the previous expression becomes:

$$n = G/BM \propto i_{ph}$$

We can therefore observe a linear behavior between the photocurrent and the light intensity received by the sample (example of sample n°1 where the number of impurities must be important compared to the other phases). In addition, when the luminous flux increases, the value of n_{pe} becomes greater than that of M and the expression takes the following form:

$$n = \sqrt{G\ /B}\ \ a\ \phi_0^{1/2}$$

The system gradually switches from a linear behavior to a square root behavior hence the evolution in power law (which is observed for samples n° 2, n°3 and n°4 where the density of the photoelectrons produced is higher than that of impurities). This model explains the experimental observations.

Table 7. Fit parameters of the power law applied on phases *1→4.*

$y = \beta*x^\gamma$	Phase 1	Phase 2	Phase 3	Phase 4
β	0.00952 ± 0.00121	0.0139 ± 0.0025	0.00427 ± 7.70304E-4	0.06952 ± 0.0226
γ	0.91517 ± 0.02798	0.71843 ± 0.04012	0.80475 ± 0.04003	0.74296 ± 0.07235
R	0.99735	0.99033	0.99271	0.97225
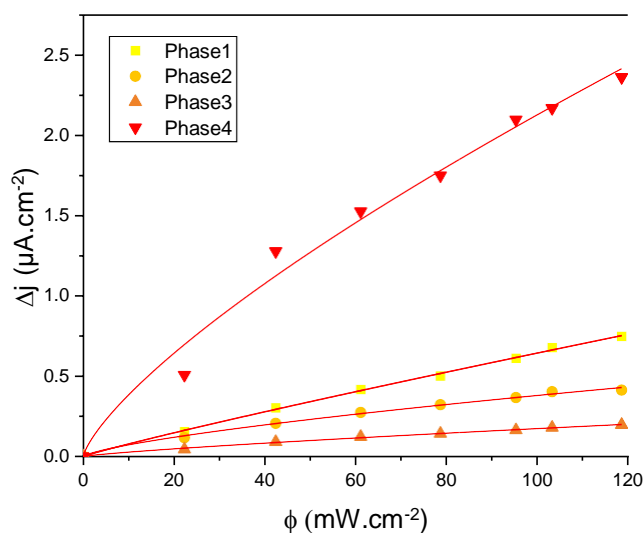
Figure 9. The variation of current density (Δj) as a function of light intensity for phases 1→4.

Conclusion

The new $Ba_5(VO_{4-\alpha}S_\alpha)_3X$ (X= F, Cl, I) series was designed by replacing vanadate groups with thiovanadate groups in the known apatite series $Ba_5(VO_4)_3X$ (X= F, Cl, I), thus leading to triple-anion lattices. Compared to well-known apatites, the presence of thiovanadates makes them the first halide-thio-apatites. The light absorption characterizations show a visible light response for powders with X= F and Cl which make these materials promising for solar photoelectric and photocatalytic applications. For X= I, single crystals were identified but additional synthetic efforts are required to reach a high purity powder for photoelectric measurements. While the single crystal composition for $Ba_5(VO_4)_3F$ corresponds well to the pure powder, for the Cl-phases, the O/S ratios refined for single crystals diverge from the simple nominal targeted powder compositions. Indeed, from one synthesis to the other, three different O/S ratios in three different crystals were refined. It shows both the versatility and the opportunity to easily modify the O/S ratio as well as the difficulty to control the stoichiometry of such crystals. Here the observation that crystal growth may occur with a slight divergence of the stoichiometry compared to the bulk is yet to understand.

The displacement of the light absorption range toward the visible range compared to other

24

apatite analogues is induced by the contribution of sulfur states at the top of the valence band which is raised. We show that those phases may be suitable candidates as photocatalysts for solar water-splitting reaction. This study reveals the great versatility of this system for tuning finely the bandgap by playing concomitantly with the vanadium O/S coordination ratio and the halide anion typewithin the channels. Multiple possibilities are opened knowing that the cationic sites might be also substituted. Substitution of the halide site by Br and higher O/S ratio in the thiovanadates are under investigation.

Supplementary information: Reconstructed prescessions images (Figure S1)**,** additional powder XRD refinement of phase 1 ($Ba_5(VO_3S)_3F$) (Figure S2), band structures (Figure S3), total density of states (Figure S4 and S5). Table S1 (EDS analysis) and Table S2-S3 (Anisotropic thermal parameters). **CCDC database deposition Numbers**: **2247595** for $Ba_5V_3O_{9.102}S_{2.898}Cl$ (cristal C1), **2247597** for $Ba_5V_3O_{8.552}S_{3.448}Cl$ (cristal C2), **2247599** for $Ba_5V_3O_{7.869}S_{4.131}Cl$ (cristal C3), **2245835** for $Ba_5(VO_3S)_3F$ (C4).

References

(1) Ai-Mamouri, M.; Edwards, P. P.; Greaves, C.; Slaski, M. Synthesis and Superconducting Properties of the Strontium Copper Oxy-Fluoride Sr2CuO2F2+δ. *Nature* **1994**, *369* (6479), 382–384. https://doi.org/10.1038/369382a0.

(2) Li, Y.-Y.; Wang, W.-J.; Wang, H.; Lin, H.; Wu, L.-M. Mixed-Anion Inorganic Compounds: A Favorable Candidate for Infrared Nonlinear Optical Materials. *Cryst. Growth Des.* **2019**, *19* (7), 4172–4192. https://doi.org/10.1021/acs.cgd.9b00358.

(3) Palazzi, M.; Carcaly, C.; Laruelle, P.; Flahaut, J. Crystal Structure and Properties of (LaO) CuS and (LaO) AgS BT - The Rare Earths in Modern Science and Technology: Volume 3; McCarthy, G. J., Silber, H. B., Rhyne, J. J., Kalina, F. M., Eds.; Springer US: Boston, MA, 1982; pp 347–350. https://doi.org/10.1007/978-1-4613-3406-4_72.

(4) Valldor, M.; Adler, P.; Prots, Y.; Burkhardt, U.; Tjeng, L. H. S = 2 Spin Ladders in the Sulfide Oxide BaFe 2 S 2 O (Eur. J. Inorg. Chem. 36/2014). *Eur. J. Inorg. Chem.* **2014**, *2014* (36). https://doi.org/10.1002/ejic.201490172.

(5) Kageyama, H.; Hayashi, K.; Maeda, K.; Attfield, J. P.; Hiroi, Z.; Rondinelli, J. M.; Poeppelmeier, K. R. Expanding Frontiers in Materials Chemistry and Physics with Multiple Anions. *Nat. Commun.* **2018**, *9* (1), 772. https://doi.org/10.1038/s41467-018-02838-4.

(6) Miyoshi, A.; Maeda, K. Recent Progress in Mixed-Anion Materials for Solar Fuel Production. *Sol. RRL* **2021**, *5* (6), 2000521. https://doi.org/10.1002/solr.202000521.

(7) Wang, Q.; Nakabayashi, M.; Hisatomi, T.; Sun, S.; Akiyama, S.; Wang, Z.; Pan, Z.; Xiao, X.; Watanabe, T.; Yamada, T.; Shibata, N.; Takata, T.; Domen, K. Oxysulfide Photocatalyst for Visible-Light-Driven Overall Water Splitting. *Nat. Mater.* **2019**, *18* (8), 827–832. https://doi.org/10.1038/s41563-019-0399-z.

(8) Kabbour, H.; Sayede, A.; Saitzek, S.; Lefèvre, G.; Cario, L.; Trentesaux, M.; Roussel, P. Structure of the Water-Splitting Photocatalyst Oxysulfide α-LaOInS 2 and Ab Initio Prediction of New Polymorphs. *Chem. Commun.* **2020**, *56* (11), 1645–1648. https://doi.org/10.1039/C9CC09797J.

(9) Almoussawi, B.; Huvé, M.; Dupray, V.; Clevers, S.; Duffort, V.; Mentré, O.; Roussel, P.; Arevalo-Lopez, A. M.; Kabbour, H. Oxysulfide Ba 5 (VO 2 S 2) 2 (S 2) 2 Combining Disulfide Channels and Mixed-Anion Tetrahedra and Its Third-Harmonic-Generation Properties. *Inorg. Chem.* **2020**, *59* (9), 5907–5917. https://doi.org/10.1021/acs.inorgchem.9b03674.

(10) Almoussawi, B.; Kageyama, H.; Roussel, P.; Kabbour, H. Versatile Interplay of Chalcogenide and Dichalcogenide Anions in the Thiovanadate Ba 7 S(VS 3 O) 2 (S 2) 3 and Its Selenide Derivatives: Elaboration and DFT Meta-GGA Study. *ACS Org. Inorg. Au* **2023**, *3* (3), 158–170. https://doi.org/10.1021/acsorginorgau.3c00006.

(11) Nicoud, S.; Mentré, O.; Kabbour, H. The Ba 10 S(VO 3 S) 6 Oxysulfide: One-Dimensional Structure and Mixed Anion Chemical Bonding. *Inorg. Chem.* **2019**, *58* (2), 1349–1357. https://doi.org/10.1021/acs.inorgchem.8b02893.

(12)   Al Bacha, S.; Saitzek, S.; McCabe, E. E.; Kabbour, H. Photocatalytic and Photocurrent Responses to Visible Light of the Lone-Pair-Based Oxysulfide Sr 6 Cd 2 Sb 6 S 10 O 7. *Inorg. Chem.* **2022**, *61* (46), 18611–18621. https://doi.org/10.1021/acs.inorgchem.2c03040.

(13)   Knyazev, A. V.; Chernorukov, N. G.; Bulanov, E. N. Apatite-Structured Compounds: Synthesis and High-Temperature Investigation. *Mater. Chem. Phys.* **2012**, *132* (2–3), 773–781. https://doi.org/10.1016/j.matchemphys.2011.12.011.

(14)   Nakamura, M.; Oqmhula, K.; Utimula, K.; Eguchi, M.; Oka, K.; Hongo, K.; Maezono, R.; Maeda, K. Light Absorption Properties and Electronic Band Structures of Lead-Vanadium Oxyhalide Apatites Pb 5 (VO 4) 3 X (X=F, Cl, Br, I). *Chem. – An Asian J.* **2020**, *15* (4), 540–545. https://doi.org/10.1002/asia.201901692.

(15)   Petříček, V.; Dušek, M.; Palatinus, L. Crystallographic Computing System JANA2006: General Features. *Zeitschrift für Krist. - Cryst. Mater.* **2014**, *229* (5), 345–352. https://doi.org/10.1515/zkri-2014-1737.

(16)   van der Lee, A. Charge Flipping for Routine Structure Solution. *J. Appl. Crystallogr.* **2013**, *46* (5), 1306–1315. https://doi.org/10.1107/S0021889813020049.

(17)   Roh, Y.-H.; Hong, S.-T. Apatite-Type Ba 5 (VO 4) 3 Cl. *Acta Crystallogr. Sect. E Struct. Reports Online* **2005**, *61* (8), i140–i142. https://doi.org/10.1107/S1600536805018854.

(18)   Wong, C. J.; Hopkins, E. J.; Prots, Y.; Hu, Z.; Kuo, C.-Y.; Pi, T.-W.; Valldor, M. Anionic Ordering in Ba 15 V 12 S 34 O 3 , Affording Three Oxidation States of Vanadium and a Quasi-One-Dimensional Magnetic Lattice. *Chem. Mater.* **2016**, *28* (6), 1621–1624. https://doi.org/10.1021/acs.chemmater.6b00187.

(19)   Kang, J.; Yang, Y.; Pan, S.; Yu, H.; Zhou, Z. Synthesis, Crystal Structure and Optical Properties of Ba5V3O12F. *J. Mol. Struct.* **2014**, *1056–1057*, 79–83. https://doi.org/10.1016/j.molstruc.2013.10.009.

(20)   Tauc, J.; Grigorovici, R.; Vancu, A. Optical Properties and Electronic Structure of Amorphous Germanium. *Phys. status solidi* **1966**, *15* (2), 627–637. https://doi.org/10.1002/pssb.19660150224.

(21)   Kubelka, P. and Munk, F. Ein Beitrag Zur Optik Der Farbanstriche. Zeitschrift Für Technische Physik. *Techn. Phys.* **1931**, *12*, 593–601.

(22)   Tauc, J.; Grigorovici, R.; Vancu, A. Optical Properties and Electronic Structure of Amorphous Germanium. *Phys. status solidi* **1966**, *15* (2), 627–637. https://doi.org/10.1002/pssb.19660150224.

(23)   Matsumoto, Y. Energy Positions of Oxide Semiconductors and Photocatalysis with Iron Complex Oxides. *J. Solid State Chem.* **1996**, *126* (2), 227–234. https://doi.org/10.1006/jssc.1996.0333.

(24)   Butler, M. A.; Ginley, D. S. Prediction of Flatband Potentials at Semiconductor-Electrolyte Interfaces from Atomic Electronegativities. *J. Electrochem. Soc.* **1978**, *125* (2), 228–232. https://doi.org/10.1149/1.2131419.

(25)   Xu, Y.; Schoonen, M. A. A. The Absolute Energy Positions of Conduction and Valence Bands of Selected Semiconducting Minerals. *Am. Mineral.* **2000**, *85* (3–4), 543–556. https://doi.org/10.2138/am-2000-0416.

(26) Castelli, I. E.; Olsen, T.; Datta, S.; Landis, D. D.; Dahl, S.; Thygesen, K. S.; Jacobsen, K. W. Computational Screening of Perovskite Metal Oxides for Optimal Solar Light Capture. *Energy Environ. Sci.* **2012**, *5* (2), 5814–5819. https://doi.org/10.1039/C1EE02717D.

(27) Hussein, F. Photochemical Treatments of Textile Industries Wastewater. *Asian J. Chem.* **2012**, *24*, 5427–5434.

(28) Herrmann, J.-M. Heterogeneous Photocatalysis: Fundamentals and Applications to the Removal of Various Types of Aqueous Pollutants. *Catal. Today* **1999**, *53* (1), 115–129. https://doi.org/10.1016/S0920-5861(99)00107-8.

(29) Jin, S. F.; Huang, Q.; Lin, Z. P.; Li, Z. L.; Wu, X. Z.; Ying, T. P.; Wang, G.; Chen, X. L. Two-Dimensional Magnetic Correlations and Partial Long-Range Order in Geometrically Frustrated CaOFeS with Triangle Lattice of Fe Ions. *Phys. Rev. B* **2015**, *91* (9), 094420. https://doi.org/10.1103/PhysRevB.91.094420.

(30) Ullrich, B.; Xi, H. Photocurrent Limit in Nanowires. *Opt. Lett.* **2013**, *38* (22), 4698. https://doi.org/10.1364/OL.38.004698.